

Exploring mission design for imaging spectroscopy retrievals for land and aquatic ecosystems

Ann Raiho¹, Kerry Cawse-Nicholson², Adam Chlus³, Jeff Dozier⁴, Michelle M. Gierach², Kimberley Miner³, Shawn Paul Serbin⁵, David Schimel³, Fabian Schneider⁶, Alexey N Shiklomanov¹, S. McKenzie Skiles⁷, David Ray Thompson², Philip Townsend³, Shannon-Kian Zareh², and Benjamin Poulter⁸

¹NASA Goddard Space Flight Center

²Jet Propulsion Laboratory, California Institute of Technology

³Jet Propulsion Laboratory

⁴University of California, Santa Barbara

⁵Brookhaven National Laboratory (DOE)

⁶California Institute of Technology

⁷University of Utah

⁸NASA

November 23, 2022

Abstract

The retrieval algorithms used for optical remote sensing satellite data to estimate Earth's geophysical properties have specific requirements for spatial resolution, temporal revisit, spectral range and resolution, and instrument signal to noise ratio (SNR) performance to meet science objectives. Studies to estimate surface properties from hyperspectral data use a range of algorithms sensitive to various sources of spectroscopic uncertainty, which are in turn influenced by mission architecture choices. Retrieval algorithms vary across scientific fields and may be more or less sensitive to mission architecture choices that affect spectral, spatial, or temporal resolutions and spectrometer SNR. We used representative remote sensing algorithms across terrestrial and aquatic study domains to inform aspects of mission design that are most important for impacting accuracy in each scientific area. We simulated the propagation of uncertainties in the retrieval process including the effects of different instrument configuration choices. We found that retrieval accuracy and information content degrade consistently at >10 nm spectral resolution, >30 m spatial resolution, and >8 day revisit. In these studies, the noise reduction associated with lower spatial resolution improved accuracy vis à vis high spatial resolution measurements. The interplay between spatial resolution, temporal revisit and SNR can be quantitatively assessed for imaging spectroscopy missions and used to identify key components of algorithm performance and mission observing criteria.

1 **Exploring mission design for imaging spectroscopy retrievals for land and aquatic**
2 **ecosystems**

3 **A. M. Raiho^{1 2}, K. Cawse-Nicholson³, A. Chlus³, J. Dozier⁴, M. Gierach³, K. Miner³, F.**
4 **Schneider³, D. Schimel³, S. Serbin⁶, A. N. Shiklomanov¹, D. R. Thompson³, P. A.**
5 **Townsend^{3 5}, S. Zareh³, M. Skiles⁷, B. Poulter¹**

6 ¹NASA Goddard Space Flight Center, Biospheric Sciences Lab, Greenbelt, MD 20771

7 ²Earth System Science Interdisciplinary Center, University of Maryland, College Park, MD
8 20740

9 ³Jet Propulsion Laboratory, California Institute of Technology, Pasadena, CA 91109

10 ⁴Bren School of Environmental Science & Management, University of California, Santa Barbara,
11 CA 93106

12 ⁵University of Wisconsin – Madison, , Department of Forest and Wildlife Ecology, 1630 Linden
13 Drive, Madison, WI 53706 USA

14 ⁶Brookhaven National Laboratory, Upton, NY 11973

15 ⁷Department of Geography, University of Utah, Salt Lake City, UT 84112

16 Corresponding author: Ann Raiho (ann.m.raiho@nasa.gov)

17 **Key Points:**

- 18 • High spectral resolution (~10nm), high spatial resolution (~30m), and high revisit (less
19 than 16 days) is needed to estimate Earth's geophysical properties with imaging
20 spectroscopy and corresponding retrieval algorithms.
- 21 • We simulate the effects of instrument signal-to-noise ratios (SNR) on retrieval accuracy
22 using a codebase called Hypertrace.
- 23 • Our approach provides a framework for current and future mission design planning.

24 **Abstract**

25 The retrieval algorithms used for optical remote sensing satellite data to estimate Earth's
26 geophysical properties have specific requirements for spatial resolution, temporal revisit, spectral
27 range and resolution, and instrument signal to noise ratio (SNR) performance to meet science
28 objectives. Studies to estimate surface properties from hyperspectral data use a range of
29 algorithms sensitive to various sources of spectroscopic uncertainty, which are in turn influenced
30 by mission architecture choices. Retrieval algorithms vary across scientific fields and may be
31 more or less sensitive to mission architecture choices that affect spectral, spatial, or temporal
32 resolutions and spectrometer SNR. We used representative remote sensing algorithms across
33 terrestrial and aquatic study domains to inform aspects of mission design that are most important
34 for impacting accuracy in each scientific area. We simulated the propagation of uncertainties in
35 the retrieval process including the effects of different instrument configuration choices. We
36 found that retrieval accuracy and information content degrade consistently at >10 nm spectral
37 resolution, >30 m spatial resolution, and >8 day revisit. In these studies, the noise reduction
38 associated with lower spatial resolution improved accuracy vis à vis high spatial resolution
39 measurements. The interplay between spatial resolution, temporal revisit and SNR can be
40 quantitatively assessed for imaging spectroscopy missions and used to identify key components
41 of algorithm performance and mission observing criteria.

42 **Plain Language Summary**

43 Detailed observations of Earth's visible to shortwave infrared spectra, known as hyperspectral
44 imagery or imaging spectroscopy, will provide novel insights across scientific disciplines.
45 Vegetation, aquatic, mineral, and snow scientists have independently developed techniques for
46 using hyperspectral imagery to measure different features of their targets. But, developing
47 measurement objectives that will work well for every kind of measurement target is difficult.
48 Here, we test several representative image analysis techniques to inform the planning process
49 future hyperspectral missions. Specifically, we investigate the effect that changing the number of
50 spectral bands, the size of image pixels, and the frequency of repeat observations has on each
51 technique's accuracy.

52 **1 Introduction**

53 Global imaging spectroscopy from NASA's Surface Biology and Geology (SBG) designated
54 observable will improve understanding of five focal areas of Earth Science: marine and
55 terrestrial ecosystems, seasonal to centennial climate variability, weather and air quality,
56 hydrology and water resources, and dynamics and hazards associated with Earth's surface and
57 interior (National Academies of Sciences, Engineering, and Medicine, 2018; Schimel,
58 Townsend and Pavlick, 2020). SBG will provide visible through shortwave-infrared reflectance
59 (~380-2500 nm wavelengths) and thermal (4.5 to 12 μm) emissivity observations from space
60 with global coverage, frequent revisit, and high spectral fidelity (Stavros et al., in press).
61 Designing a successful mission that meets diverse scientific objectives requires evaluating
62 alternative mission architectures (Thompson *et al.*, 2021). In SGB's case, each science focal area
63 depends on a different aspect of mission architecture for accuracy (Cawse-Nicholson *et al.*,
64 2021). To characterize the scientific impact of trade-offs associated with different mission
65 architectures, we illustrate the driving examples behind each focal area (Table 1) and assess the
66 effects of measurement trades on a target retrieval.

67 Trade-offs are a fundamental component of mission design. Fundamental trade-offs associated
68 with different mission architectures occur between spectral, spatial, and temporal resolutions and
69 the radiometric precision of the instrument. Radiometric precision (i.e., signal-to-noise ratio or
70 SNR) is a function of the number of photons an instrument receives. When integrating over a
71 smaller spectral (i.e., higher spectral resolution) or spatial area (i.e., higher spatial resolution) at
72 the fixed orbital speed of a spacecraft, fewer photons will reach the instrument, degrading SNR
73 with downstream consequences for retrievals of geophysical variables. On the other hand, some
74 features of interest require fine spectral and spatial resolution to be accurately retrieved. Mission
75 architecture design must address how optimizing for high instrument SNR impacts spectral,
76 spatial, and temporal resolution. For a mission like SBG, which covers a range of scientific
77 disciplines, the trades between each of the three types of resolutions and SNR must be
78 thoroughly evaluated using a consistent traceability framework.

79 Imaging spectroscopy (i.e., 100s to 1000s of contiguous wavelength channels) allows for more
80 precise discrimination of Earth surface properties than multispectral imagery (i.e., 3 to 20
81 wavelength channels) because of the higher information content in these hyperspectral
82 measurements (Thompson, Boardman, *et al.*, 2017; Cawse-Nicholson *et al.*, 2019). The spectral
83 resolution of a hyperspectral image has been shown to greatly affect mineral (Swayze, 2003) and
84 vegetation (Shiklomanov *et al.*, 2016) retrieval accuracy because these algorithms require fine
85 spectrally resolved information. In both these cases, high spectral resolution may compensate for
86 lower SNR by contributing more information content. Requirements also vary considerably by
87 algorithm type. For example, snow retrieval algorithms are similar to common mineral retrieval
88 algorithms that consider the spectral signature around known absorption wavelengths (Nolin and
89 Dozier, 1993). As such, a stronger focus on fine spectral resolution is needed to discriminate and
90 identify key mineral absorption features associated with specific mineral species or to identify or
91 discriminate dust versus snow grain particles, as well as determine water content and age of
92 snowpack (REFS). On the other, vegetation algorithms are typically based on statistical models
93 (e.g., Partial Least Squares Regression, PLSR; Burnett *et al.*, 2021) or physically-based models
94 (e.g., radiative transfer model inversion) that relate plant properties at leaf or canopy level to
95 more broad absorption features (e.g. Curran, 1989) and spectral information (Verrelst *et al.*,
96 2019; Serbin and Townsend, 2020) As such, vegetation algorithms tend to require higher SNR or
97 spatial resolution over very fine spectral resolution. Aquatic algorithms are especially sensitive to
98 the additive atmospheric contribution to the spectral signal, and their retrieval accuracy may be
99 particularly susceptible to degrading spectral resolution and the effects of low SNR because of
100 how aquatic properties such as glint (Hu, 2011), bubbles (Dierssen, 2019), and optical variability
101 in the water column (Garcia *et al.*, 2020) interact with water-leaving radiances. In our analyses,
102 we demonstrate how retrieval algorithms that depend on hyperspectral imagery respond to the
103 effects of degrading spectral resolution and radiometric precision on retrieval accuracy.

104 Holding SNR constant, finer spatial resolution or increased number of pixels per image will
105 typically lead to higher information content in an image (Cawse-Nicholson *et al.*, 2019).
106 However, instrument SNR decreases with finer spatial resolution because smaller pixels result in
107 fewer photons received by each focal plane array detector element. A driving case for spatial
108 resolution is the ecological focal area where different ecosystems have different dominant
109 spatial scale processes (Turner, Dale and Gardner, 1989; Wang *et al.*, 2018). For instance, a
110 homogenous scenes (e.g., dense deciduous forest) may not require fine spatial detail to

111 understand plant functional traits while a heterogeneous scenes (e.g., sparse lower montane
112 ecosystem) with a variety of ecosystem types may require fine spatial detail.

113 Frequent temporal revisit is another fundamental aspect of the mission architecture and provides
114 a basis for quantifying the effects of natural disasters and seasonal phenomena (Schimel,
115 Townsend and Pavlick, 2020). The ability to detect a short duration event (e.g., a volcanic
116 eruption or mudslide) or frequent changes during a season (e.g., snow albedo) may be hindered
117 by longer revisit time intervals or areas where cloud cover is common, or by overpass time.
118 However, increasing revisit frequency can be obtained at the cost of spatial resolution and must
119 be quantitatively justified.

120 To optimize for retrieval accuracy across five scientific areas, mission architecture design must
121 consider tradeoffs between spectral, spatial, and temporal resolutions. In this study, we look at
122 specific driving case studies to quantify the performance impacts of these design choices on the
123 range of SBG science objectives. Specifically, we perform a simulation experiment in which we
124 synthesize artificial imaging spectroscopy data and apply state of practice retrieval algorithms
125 with varying sensor noise and resolution. Currently, high resolution hyperspectral time series
126 data are uncommon, so our strategy is to show the probability of detecting an event depending on
127 event duration and revisit time interval using simulated data. Our approach compares algorithm
128 accuracy with and without instrument noise along gradients of coarsening resolutions to
129 determine optimal resolutions for imaging spectroscopy architecture design.

130 **2 Materials and Methods**

131 Radiance measurements from hyperspectral missions will be converted into surface reflectance
132 values through atmospheric correction, which isolates and removes the contribution of
133 absorption and scattering from atmospheric aerosols, water vapor, and other components on the
134 overall radiance signal, and provides estimates of incoming and outgoing radiation for each pixel
135 at the Earth surface (Vermote and Kotchenova, 2008). In this study, we use an atmospheric
136 correction approach that employs a physically based atmospheric radiative transfer model
137 inversion. We use the Imaging Spectrometer Optimal FITting codebase (i.e., ISOFIT; Thompson
138 *et al.*, 2018), whereby atmospheric and surface reflectance can be estimated jointly using optimal
139 estimation (OE; Thompson *et al.*, 2018). Estimated surface reflectance from the OE procedure
140 then provides the information for algorithms that retrieve geophysical properties. These
141 algorithms can take many forms. The retrieval algorithms listed in Table 1 were chosen to span
142 each of the five core scientific areas and were made available through collaborations with the
143 algorithms working group.

144 2.1 Hypertrace and instrument modeling

145 We developed the Hypertrace simulation workflow to trace the hyperspectral data
146 uncertainty pipeline from top of atmosphere radiance to bio- and geophysical retrievals
147 (<https://github.com/isofit/isofit/tree/master/examples/py-hypertrace>). Operationally,
148 Hypertrace starts from known surface reflectance and atmospheric conditions based on a
149 specific spectral resolution, and then simulates top-of-atmosphere radiance and
150 instrument radiances based on the proposed instrument design, and then performs
151 atmospheric correction via optimal estimation to estimate surface reflectance.

152 Pragmatically, Hypertrace is a wrapper around the ISOFIT codebase (See: Brodrick et al,
 153 2021) which provides both forward and inverse reflectance modeling for translation
 154 between reflectance and radiance. Our ISOFIT configuration files can be found in the
 155 supplemental materials. Hypertrace manages this simulation process at runtime, and
 156 applies geophysical retrieval algorithms to the estimated surface reflectance. Hypertrace
 157 is written in Python and can be configured with a simple JSON interface.

158 Hypertrace allows for the inclusion of different imaging spectrometer detector
 159 configurations that provide various SNR profiles (Figure 1). An imaging spectrometer
 160 includes the optical system and the detector. The optics include the telescope, a
 161 dispersive element such as a prism or diffraction grating, and the slit, the entrance width
 162 that determines photon throughput. In our experiments, we used configurations for two
 163 Chroma instruments (i.e., focal plane array) Instrument-A and Instrument-B detectors and
 164 also Hyperion, where Instrument-A has a detector pixel pitch of 0.0030 cm and a slit
 165 width of 30 microns while Instrument-B has a detector pixel pitch of 0.0018 cm and a slit
 166 width of 18 microns. We selected these Chroma spectrometers as examples because they
 167 have been used in the Earth Surface Mineral Dust Source Investigation (EMIT) mission,
 168 a similar imaging spectroscopy mission to SBG (Connelly *et al.*, 2021). We compare
 169 against Hyperion to show the abilities of our workflow to include SNR from both future
 170 and past instruments. These spectrometer settings as well as desired instrument spatial
 171 resolution alter the SNR along the visible to shortwave infrared (Figure 1).

172 For the Chroma instruments, we derived instrument SNR using the following approach.
 173 The SNR describes the ratio of the signal to noise for the given spatial resolution element,
 174 where the signal is defined as the total number of collected electrons per unit area (i.e.
 175 pixel) over the total noise for the same area. The signal is proportional to the following
 176 equation:

$$177 \text{Signal} = L * \delta\lambda * A_o * \Omega_d * t_{int} * T * \eta \quad (1)$$

178 Where L is spectral radiance at sensor, $\delta\lambda$ is the instrument's spectral resolution, A_o is the
 179 instrument telescope aperture, Ω_d is the solid angle of the instrument, t_{int} is the integration
 180 time per spatial sample, T is transmission, and η is the detector quantum efficiency.

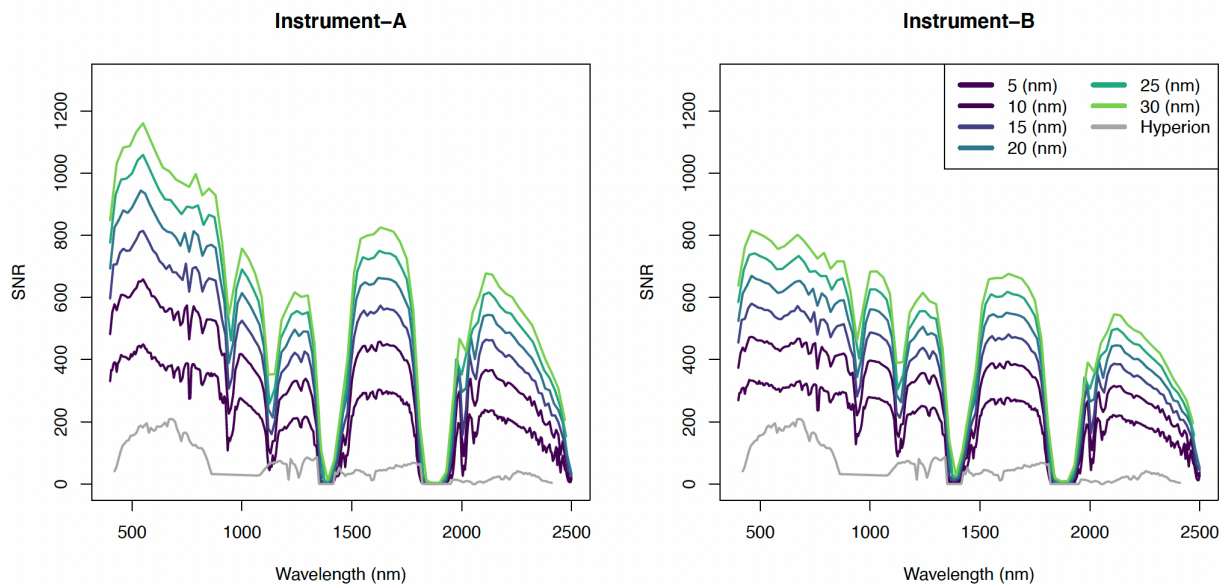
181 For a given spatial sample, the noise comes from multiple contributing factors, including
 182 the shot noise, read noise, dark noise, electronics noise and quantum noise.

$$183 \text{Noise} = \sqrt{N_{shot}^2 + N_{dark}^2 + N_{read}^2 + N_{electronics}^2} \quad (2)$$

184 The shot noise is usually the largest contributor to the noise and is a poissonian effect that
 185 is an inherent property of the photon collection phenomenon in optical devices. The
 186 dark noise is the product of the dark current of the focal plane array and the integration
 187 times we work with. The read noise is associated with every frame read. For digital focal
 188 plane array like Instrument-B the electronics noise is zero while it is a non-zero value for

189 the analog version Instrument-A. Usually the focal plane array gets characterized in a
 190 laboratory thermal-vacuum chamber that allows the read noise, dark current, well
 191 capacity, linearity and crosstalk to be measured and characterized. The results of these
 192 characterizations are critical to the design and performance predictions of imaging
 193 spectrometers using the focal plane array.

194 For the Hyperion instrument, we used a parametric approach for calculating instrument
 195 SNR. First, we collected invariant scenes from early in the Hyperion campaign. We then
 196 used the radiance from the invariant scenes and the parameter noise estimation process
 197 from Bioucas-Dias and Nascimento, 2005 to derive SNR for Hyperion.



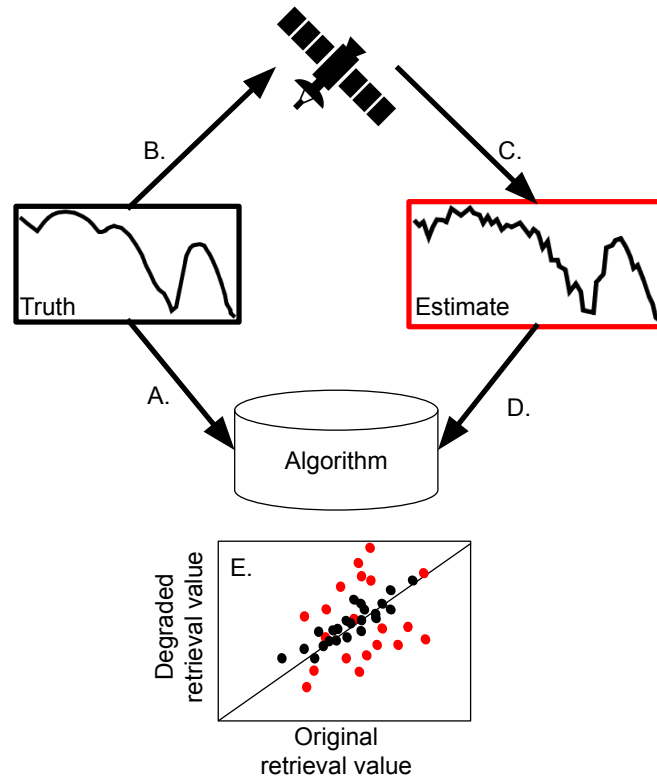
198

199 **Figure 1:** Instrument SNR over the visible and near-infrared (VNIR; 400 - 1000 nm) and short
 200 wave infrared (SWIR; 1000 - 2500 nm) for Instrument-A (left) and Instrument- (right)
 201 spectrometers colored by spatial resolution (m) range considered in this study. The vertical line
 202 in each panel represents the split between the VNIR and the SWIR.

203 2.2 Spectral and spatial sensitivity

204 Our simulation experiments have two parts: In ‘direct’ experiments, we apply retrieval
 205 algorithms to degraded reflectance data, and compare the outcome a similar retrieval at
 206 native resolution (Figure 2 black). In ‘instrument’ experiments, we degrade the radiance
 207 at sensor in Hypertrace using an instrument model, perform an atmospheric correction,
 208 and then apply the retrieval algorithm to the estimated surface reflectance. Therefore,
 209 only the instrument experiments include the effect of imperfect instrument radiometry
 210 (“noise”). We illustrate the concept behind our simulations in Figure 2. In the
 211 ‘instrument’ experiments, we consider two instrument models, representing state-of-the-
 212 art detectors due to launch in the near future (EMIT, Connelly *et al.*, 2021). We use
 213 Hypertrace to simulate the contributions of imperfect radiometry in Instrument-A,
 214 Instrument-B, or Hyperion spectrometer to biases and uncertainties in the geophysical

215 variable of interest (Figure 2 red). We repeat the direct and instrument application steps
 216 along the resolution degradation range of interest. We then compare both the direct
 217 retrievals and the Hypertrace retrievals to the direct retrieval at the native resolution using
 218 a variety of standard validation statistics, e.g., root mean square error (RMSE) and kappa
 219 score (for categorical data) to illustrate the effects of degrading resolution on retrieval
 220 accuracy.



221

222 **Figure 2:** Conceptual diagram of one iteration of our analysis. A. True surface reflectance is
 223 used to obtain true or direct retrievals that are not affected by the noise (black). B. and C. True
 224 surface reflectance is run through hypertrace forward (B) and inverse (C) models to obtain
 225 estimated surface reflectance including uncertainties from atmospheric correction and instrument
 226 design signal to noise ratio (SNR). D. These estimated reflectances (red) are given to the same
 227 algorithms and then compared to the directly estimated retrievals (E).

228 We chose spectral and spatial resolution experiments to demonstrate accuracy
 229 degradation across the full range of current mission design choices and corresponding
 230 trades with SNR. In our spectral resolution experiments, we varied the bandwidth from
 231 5nm to 30nm in 5nm increments, resulting in 6 experiments with a minimum of 70 bands
 232 and a maximum of 421 bands. Similarly, we varied spatial resolution from 20 m to 60 m
 233 by 10 m increments. We also included 100 m spatial resolution experiments to
 234 demonstrate algorithm accuracy at very low spatial resolutions. The scenes were
 235 resampled to coarser resolutions using Gaussian convolution aggregation for spectral
 236 resolution and bilinear averaging for spatial resolution (ignoring potential autocorrelation
 237 between spectral bands). We then repeated these experiments including the

238 corresponding effects of SNR shown in Figure 1 (See Figure 2 black versus red). All
 239 experiments were conducted with 1000 randomly drawn points from each scene.

240 We chose representative hyperspectral scenes based on a set of science areas where
 241 retrieval algorithms were available and provided by the algorithm developers (Table 1).
 242 These scenes have been BRDF corrected and atmospherically corrected, meaning they
 243 provide estimates of the hemispherical-directional reflectance factor (HDRF, *sensu*
 244 Schaepman-Strub et al. 2006) for a nadir viewing angle. Table 1 lists the supporting
 245 citations for each scene.

246 The algorithms use a variety of methods. Absorption feature matching uses specific
 247 features of the reflectance spectrum and measures the depth of the feature to approximate
 248 the amount of the mineral present (Swayze et. al., 2003). Benthic reflectance inversion
 249 (Thompson *et al.*, 2017) and benthic cover classifier (Hochberg and Atkinson, 2003)
 250 which we refer to together as ‘benthic cover classifier’ and least squares (Dozier and
 251 Painter, 2004) approaches rely on *in situ* data to determine which benthic cover type or
 252 snow grain size a particular reflectance represents. PLSR also uses *in situ* data to derive
 253 coefficients that are then applied to the reflectance to retrieve a vegetation property (e.g.,
 254 leaf nitrogen mass fraction).

255

Resolution	Core science area (Scene)	Algorithm	L3 retrieval (units)
Spectral	Mineral (Cuprite, Nevada, USA; AVIRIS-C; Swayze <i>et al.</i> , 2014)	Absorption feature matching	Mineral mass fraction (unitless; i.e., spectral abundance)
	Aquatic (Arlington, Great Barrier Reef, Australia; DESIS; German Aerospace Center)	Benthic cover classifier	Benthic cover type (unitless)
	Vegetation (Western Ghats, South India; Zheng <i>et al.</i> In Review)	Partial least squares regression	Leaf nitrogen mass fraction (g/mg)
	Snow (Southern Rocky Mountains, USA; Skiles and Painter, 2017)	Least squares	Snow grain size (μm)
Spatial	Vegetation (Western Ghats, South India;	Partial least squares regression	Leaf nitrogen mass fraction (g/mg)

	Zheng <i>et al.</i> In Review)		
	Vegetation (Crested Butte, Colorado, USA; Chadwick <i>et al.</i> , 2020)	Partial least squares regression	Leaf nitrogen mass fraction (g/mg)
Temporal	Event detection (Simulation)	NA	Event (no units)

256 **Table 1:** *Experiment List.* Each row describes the components of an experiment in our study
 257 grouped by the trade study resolution of interest. If citations are applicable, they are found in
 258 parentheses.

259 2.3 Temporal revisit

260 Acquisitions with high temporal revisit for hyperspectral data are rare in airborne (i.e.,
 261 AVIRIS-NG) and spaceborne archives, including PRISMA and DESIS. Lack of high
 262 revisit hyperspectral data is problematic for assessing algorithm performance and
 263 expected event detection efficiency (Schimel, Townsend and Pavlick, 2020). To
 264 overcome this obstacle here to provide quantitative information for mission architecture
 265 design in terms of revisit, we use an analytical approach where we calculate event
 266 detection probability by dividing event duration by the revisit interval. The analytical
 267 study quantifies the amount of information missed by decreasing temporal resolution for
 268 disturbance events such as fires, volcanic eruptions or landslides, which have been listed
 269 as SBG designated observables (National Academies of Sciences, Engineering, and
 270 Medicine, 2018).

271 Satellite constellations have been proposed to increase revisit time intervals by increasing
 272 the number of instruments. We provide a brief analysis of uncertainty in a vegetation
 273 retrieval caused by instrument calibration drift. Calibration drift is the time between
 274 instrument calibration at an invariate site where the longer the time the more uncertainty
 275 from drift can be expected. For this analysis, we use calibration drift uncertainty
 276 estimates derived from AVIRIS-NG where we took a random draw from a multivariate
 277 normal with mean zero and covariance from the AVIRIS-NG estimate. We applied this
 278 draw linearly to a single radiance vector to represent how drift may increase uncertainty
 279 over time. From this set of radiances with increasing drift, we estimated surface
 280 reflectance using an ISOFIT inversion. Finally, we calculated the canopy nitrogen

281 content in the set of estimated reflectances using PLSR and compared the nitrogen
282 estimates over days since calibration by calculating the relative error percentage.

283 **3 Results**

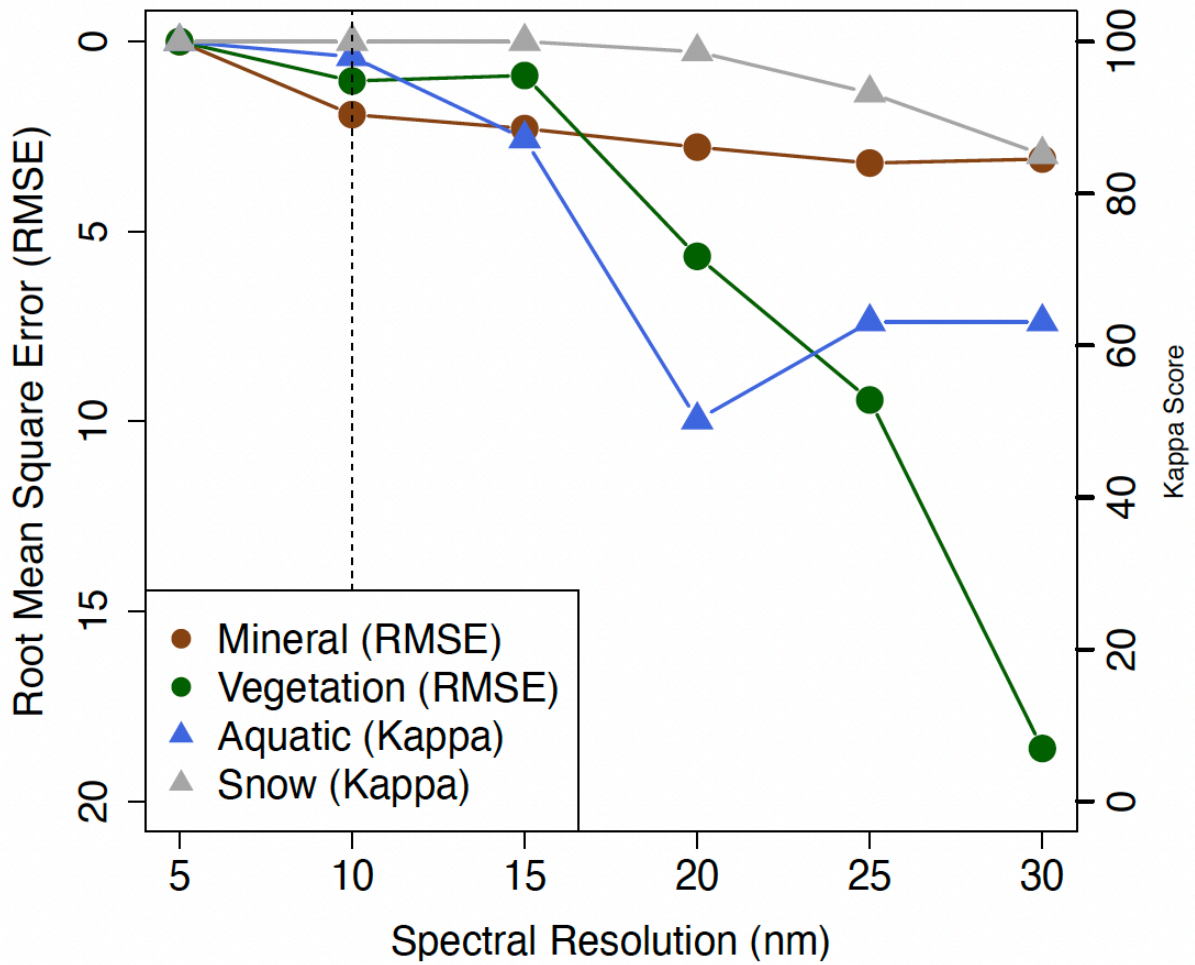
284 3.1 Spectral resolution

285 High spectral resolution (< 20 nm) resulted in greater algorithm accuracy across all
286 scientific areas in the direct algorithm application (Figure 3). The 10 nm standard
287 proposed by NASA Earth Sciences Decadal Survey (2017) provided the algorithm
288 accuracy across experiments (Figure 3 vertical dotted line). On average, vegetation PLSR
289 was the most sensitive to spectral resolution degradation, with an average RMSE change
290 of 1.7 between experiments followed by the least squares snow grain size retrieval and
291 the aquatic benthic cover classifier with an average of -8.78 and -7.38 change in kappa
292 score respectively. Least squares (i.e., snow) appears to be the least sensitive to spectral
293 resolution degradation.

294 Accuracy was not degraded significantly with the inclusion of instrument noise for the
295 mineral or aquatic spectral resolution experiments (Figure 4). Both Instrument-A and
296 Instrument-B had increased retrieval accuracy between 5nm and 10nm because of the
297 tradeoffs between SNR and spectral resolution (Figure 4a). The vegetation retrievals were
298 similar across spectral resolutions for Instrument-A and Instrument-B. However,
299 Hyperion performed poorly (i.e., RMSE = 23.54 mg/g; Figure 4b). The benthic cover
300 classifier for the aquatic spectral resolution experiment incorrectly classified the majority
301 of pixels at low spectral resolutions, classifying all pixels as algae (Figure 4c). This
302 convergence to algae classification caused a dip in the 20 nm spectral resolution
303 experiment). For the snow algorithm, SNR degraded algorithm accuracy across spectral
304 resolution experiments for both Instrument-A, Instrument-B, and Hyperion (Figure 4d).

305
306

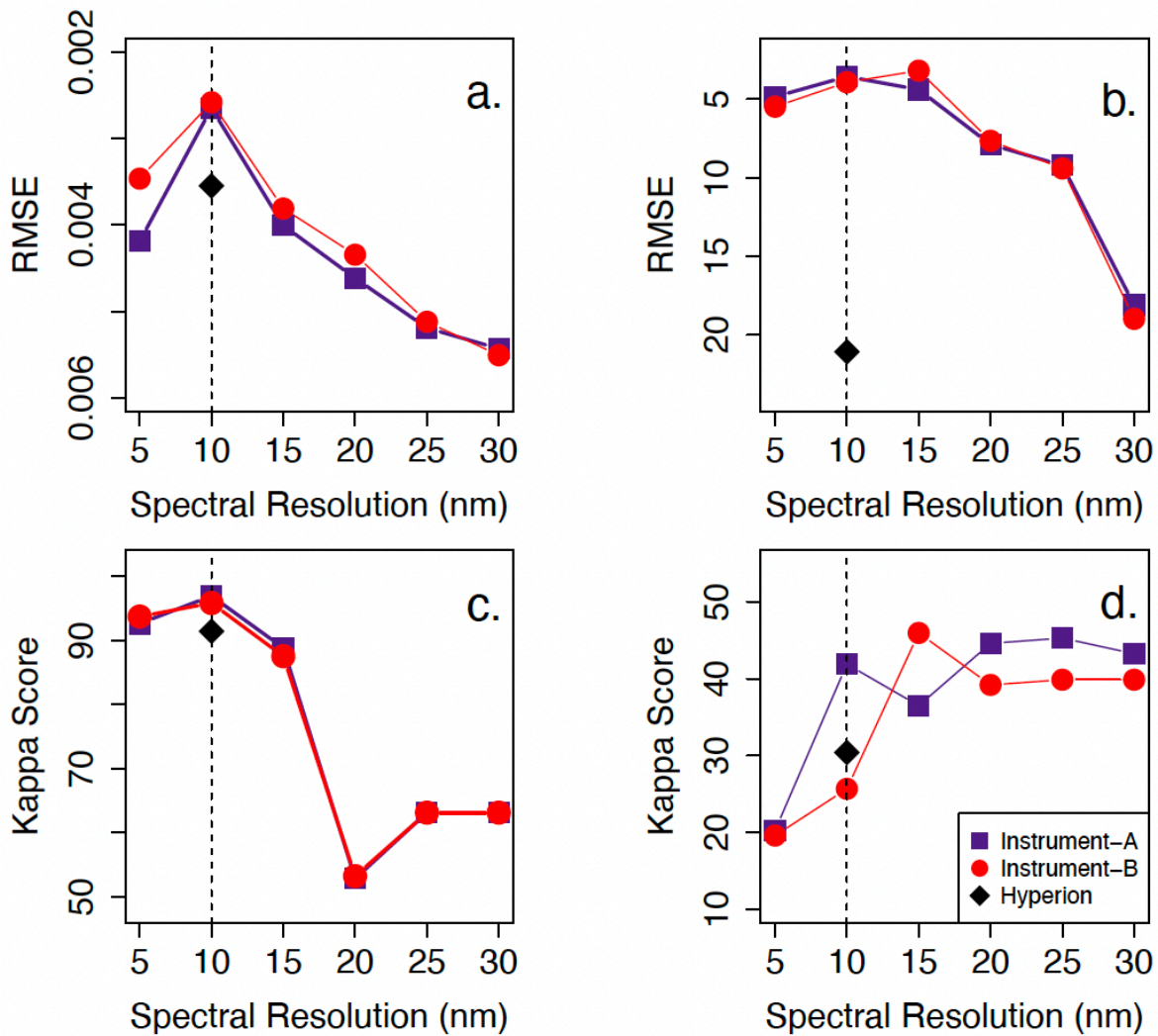
Approximately 20% of the snow spectra were categorized as having the highest snow grain size in each of the instrument application experiments.



307

308 **Figure 3:** Direct application algorithm accuracy across spectral resolution colored by scientific
 309 area. These retrievals were calculated using true reflectance and each of the retrieval algorithms.
 310 Root mean square error (RMSE) was calculated for mineral and vegetation spectra while kappa
 311 score was calculated for aquatic and snow spectra. Vertical lines represent spectral resolution

312 targets defined by the National Academies' 2017 Decadal Survey on Earth Science and
 313 Applications.



314

315 **Figure 4:** Instrument application algorithm accuracy across spectral resolution colored by
 316 scientific area for Instrument-A (purple), Instrument-B (red), and Hyperion (black) for mineral
 317 (a), vegetation (b), aquatic (c), and snow (d) retrievals. Root mean square error (RMSE) was
 318 calculated for mineral and vegetation spectra while kappa score was calculated for aquatic and
 319 snow spectra. Vertical lines represent spectral resolution targets defined by the National
 320 Academies' 2017 Decadal Survey on Earth Science and Applications.

321

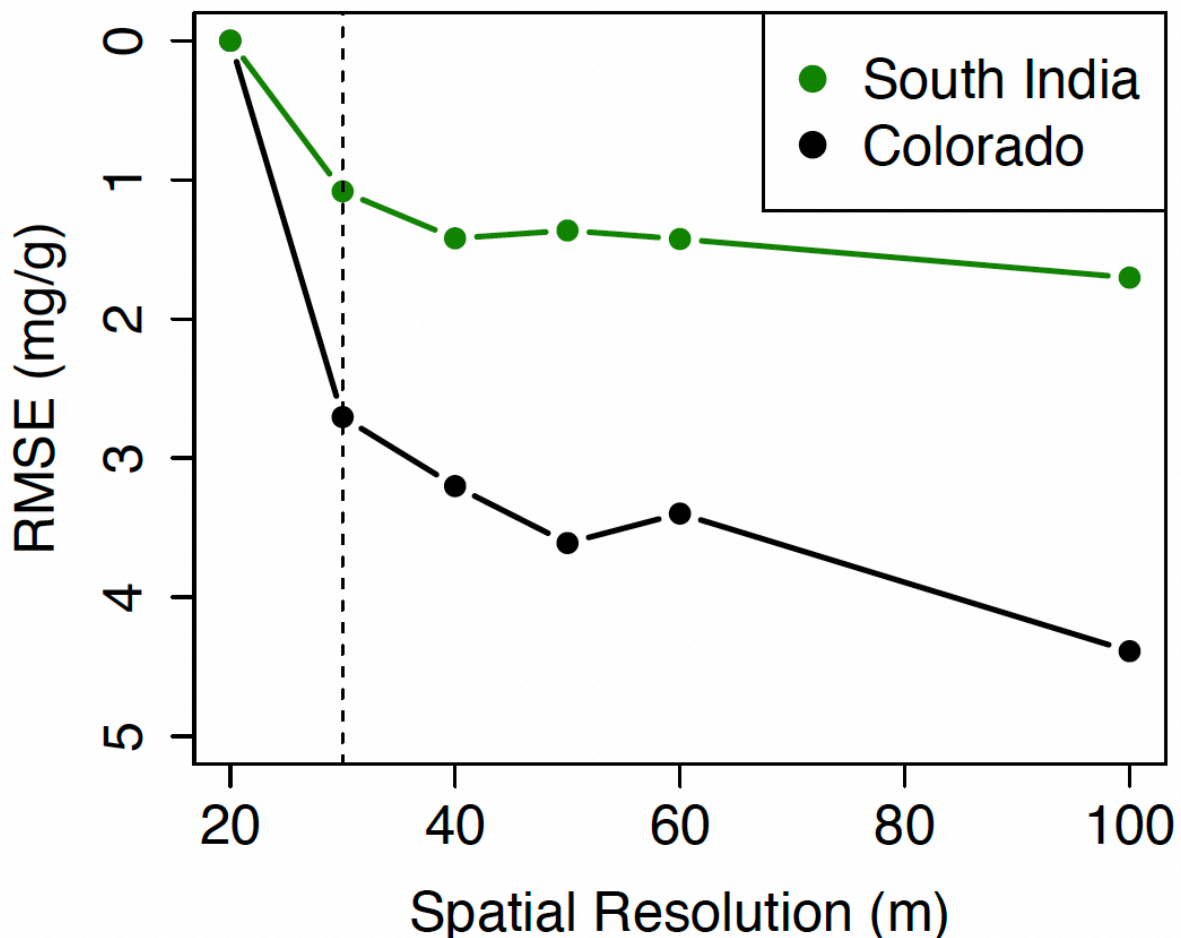
3.2 Spatial resolution

322

Retrieval accuracy decreased with coarsening spatial resolutions for both the Colorado
 323 and the South India sites in the direct application of the vegetation algorithms. Retrieval
 324 accuracy declined more quickly in the heterogeneous Colorado scene than the
 325 homogeneous South India scene (black versus green Figure 5). The 30 m standard
 326 proposed by NASA Earth Science Decadal Survey (2017) provided the most algorithm

327 accuracy across experiments (Figure 5 vertical dotted line). There was a slight increase
328 in retrieval accuracy in the state of Colorado scene between the 50 m and 60 m spatial
329 resolution experiments. We assumed this was caused by spectral mixing between
330 vegetated and non-vegetated spectra within a heterogeneous scene (Figure S3).

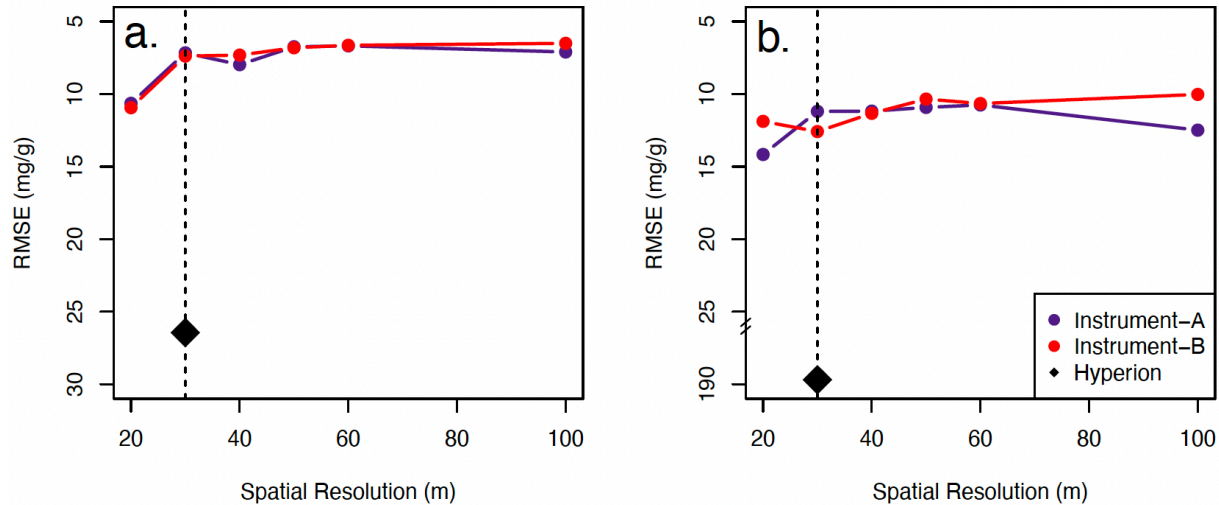
331 Instrument-A, Instrument-B, and Hyperion applications that included the affects of noise
332 both greatly decreased retrieval accuracy compared to the direct applications (Figure 6).
333 Increasing SNR over decreasing spatial resolution caused accuracy to increase somewhat
334 for both Instrument-A and Instrument-B applications, especially between 20 m and 30 m
335 spatial resolution experiments. Average SNR increased in the SWIR between instruments
336 configured for 20 m to 30 m spatial resolution by 78% SNR for Instrument-A and 81%
337 SNR for Instrument-B (Figure 1, dark purple). Hyperion was most sensitive to the PLSR
338 algorithm (Figure 4b). In comparison to both Instrument-A and Instrument-B, Hyperion
339 poorly estimated canopy nitrogen content.



340

341 **Figure 5:** Direct application algorithm accuracy calculated by root mean square error (RMSE)
342 between the degraded resolution and the native resolution across spatial resolution experiments

343 colored by scene. Vertical lines represent spectral resolution targets defined by the National
 344 Academies' 2017 Decadal Survey on Earth Science and Applications.

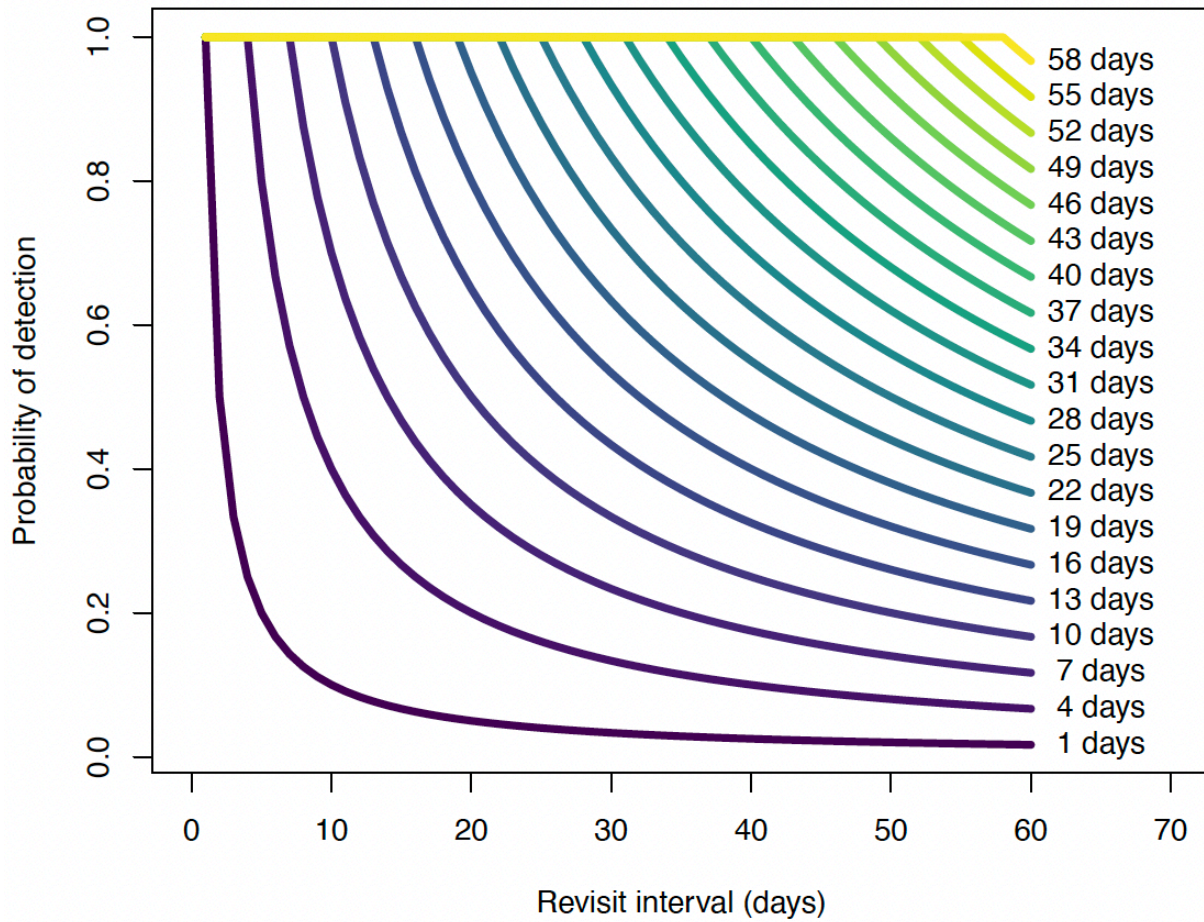


345
 346 **Figure 6:** Instrument application algorithm accuracy for South India (a) and Colorado (b) scenes.
 347 The instrument application includes the effects of noise on retrieval accuracy while the direct
 348 application (Figure 5) does not. Hyperion noise (black diamond) caused large inaccuracy in both
 349 vegetation retrievals, but especially in the Colorado scene (b). We have broken the vertical axis
 350 to include this point. Vertical lines represent spectral resolution targets defined by the National
 351 Academies' 2017 Decadal Survey on Earth Science and Applications.

352 3.3 Temporal resolution (revisit)

353 Mission revisit cadence greatly affected the probability of detecting short term events
 354 (Figure 7). Revisiting more than 20 days for a short-term event (< 5 days in duration)
 355 resulted in a probability of detection of less than 20%. Long duration events (> 21 days in
 356 duration) had a higher probability of detection even for greater than 60 day revisits
 357 (probability > 40%). Lastly, calibration drift decayed retrieval accuracy (Figure 8). Percent
 358 error reached 60% in 175 days since calibration and 100% in 300 days since calibration.

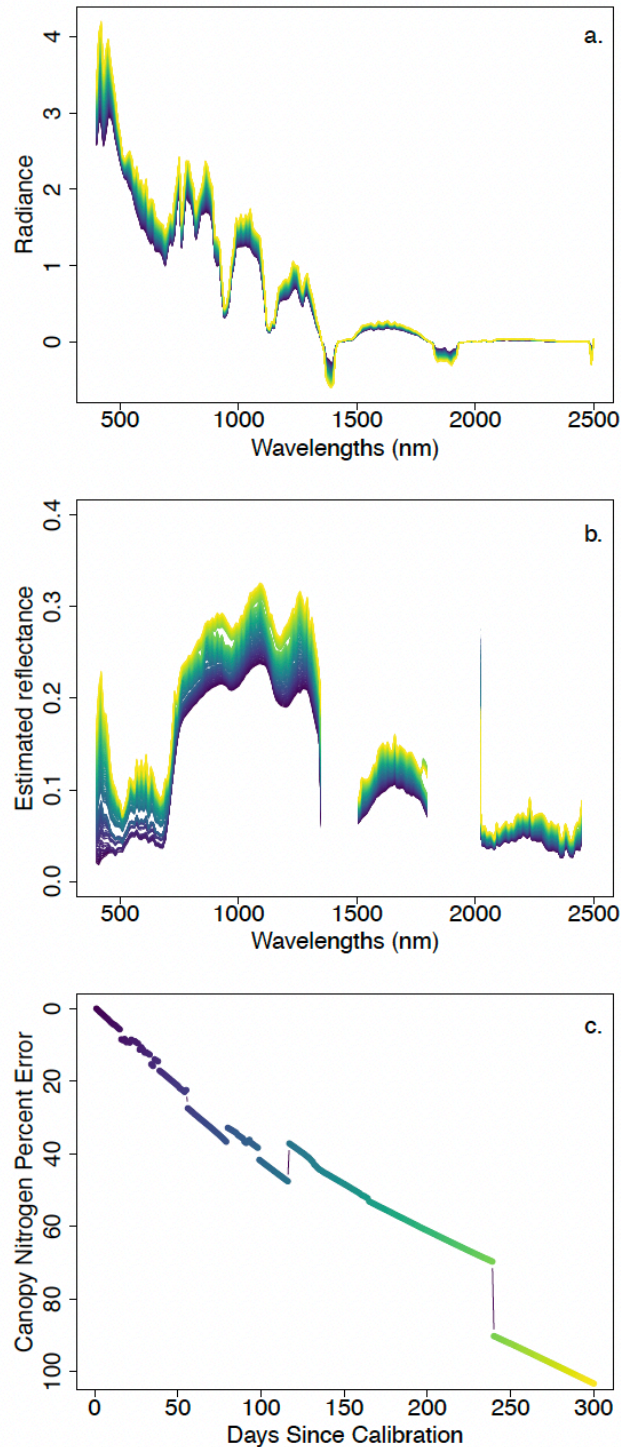
359



360

361 **Figure 7:** Detection probability as a function of increasing revisit interval colored by the
362 duration of the event where shorter events are more difficult to detect with higher revisit time
363 intervals.

364



365

366 **Figure 8:** a. Example radiances with increasing error due to drift or days since calibration. b.
367 Estimated reflectances of the radiances in (a). c. canopy nitrogen percent error as a function of
368 days since calibration. Colors in a, b, and c correspond to days since calibration.

369 **4 Discussion**

370 This suite of driving cases covering three aspects (i.e., spectral, spatial, and revisit) of mission
371 architecture interlinked with SNR and four of the five core science areas shows where high
372 resolution requirements are necessary to preserve algorithm accuracy. Our analyses confirm that
373 high spectral (~10nm), high spatial (~30m), and high revisit (less than 16 days) is needed to
374 effectively quantitatively constrain Earth's geophysical property estimation with hyperspectral
375 imagery and corresponding retrieval algorithms. We represent these targets with Figure 3
376 through 6 vertical dotted lines. Specifically, instruments with spatial resolution of 30 m and
377 spectral resolution of 10 nm obtain the largest accuracies, across the five scientific foci explored
378 here. This largely corroborates the performance proposed by the Decadal Survey in their
379 original description of the SBG mission concept. We also highlight the difference between
380 instrument choices Instrument-A and Instrument-B and past instrument Hyperion to showcase
381 how the instrument selection process may be informed by simulation experiments using
382 hypertrace or similar mission design workflows. Overall, the instruments performed similarly
383 and outperformed Hyperion (See Figure 4 and Figure 6). In the following paragraphs, we
384 elaborate on our findings for each type of resolution and finally describe our vision for the future
385 of NASA mission architecture studies.

386 We build upon previous research of mineral and vegetation retrieval algorithms (Swayze et al,
387 2003; Kokaly et al 2009; Shiklomanov *et al.*, 2016) showing that high spectral resolution
388 (~10nm) improved retrieval estimation across all scientific areas (Figure 3). In our mineral
389 assessment, we used Kaolinite absorption feature matching. This retrieval algorithm depends on
390 a narrow range of wavelengths (i.e., 2100nm - 2300nm). As the spectral resolution is coarsened,
391 the number of data points within this range decreases rapidly and results in an exponential loss of
392 information over spectral resolution. Similarly, least squares spectral matching uses a spectral
393 library as a reference for determining the amount of snow in a pixel (Dozier and Painter, 2004).
394 Aquatic benthic cover classification and vegetation PLSR algorithms use coefficients that are
395 empirically estimated using *in situ* and concurrently measured hyperspectral data, and are then
396 applied to remotely sensed imaging spectrometer data (Thompson, Hochberg, *et al.*, 2017; Serbin
397 and Townsend, 2020; Cawse-Nicholson, et al 2019) The *in situ* data are collected at a particular
398 spectral and spatial resolutions at particular locations usually during the summer months with
399 both airborne and in site data, which may ultimately drive the sensitivity of these algorithms to
400 degrading spectral resolution (e.g., Hochberg and Atkinson, 2003). More work is needed to
401 understand what the optimal sampling scheme is for both *in situ* and remotely sensed
402 hyperspectral data and how to use these data in tandem for improving aquatic classifications and
403 vegetation trait estimation algorithm retrievals.

404 Increased spatial resolution is a particularly important component for vegetation research
405 because plants operate on individual plant scales and aggregate and interact at ecosystem scale to
406 drive Earth system level phenomena (e.g., individual spruce tree to the boreal forest). Earth
407 system scientists are increasingly arguing for representing cohorts or individual level plant traits
408 and processes at a large scale to inform Earth system models (Fisher *et al.*, 2018). SBG would
409 greatly influence these models by providing a large-scale dataset at a relevant level of plant
410 organization (i.e., ~30m; Malenovsky et al, 2019). We show (Figure 4) a quantitative threshold
411 for spatial resolution from the vegetation algorithm perspective. However, both mission and
412 instrument design must be carefully constructed to include high spatial resolution and
413 accommodate physical barriers that may decrease the SNR. For the same instrument and global
414 coverage, narrower swath/field-of-view means better spatial resolution and more consistent

415 angular sampling but worse temporal resolution. So, an advance in spatial resolution may mean
416 compromising in temporal resolution. Coordinated international collaborations with other global
417 imaging spectroscopy missions (e.g. European Space Agency's Copernicus Hyperspectral
418 Imaging Mission) might provide a path forward for meeting high revisit science requirements
419 while also improving spatial resolution. Future work may focus on understanding how high
420 spatial resolution multispectral imagery informs lower spatial resolution hyperspectral trait
421 estimation to ultimately improve global vegetation trait data.

422 Altering the orbiting altitude of an instrument with a particular spatial resolution configuration
423 can increase SNR by allowing more photons to be received from a particular pixel. But, a
424 particular orbiting altitude with longer revisit intervals may not be desirable for short duration
425 event detection (Figure 6, dark purple). While our assessment relies on simulated data, it is clear
426 that increased revisit will increase the probability that events such as volcanic eruptions or
427 mudslides are detected by SBG. Extreme events are increasing with frequency as the climate
428 changes (NASA ESAS, 2016) and the effects of these types of events may be some of the most
429 important aspects of mission design to the public. Furthermore, our analysis is optimistic as it did
430 not include a source of clouds where the presence of clouds will lead to missing data and in turn
431 longer revisit. Higher revisit will enable a higher probability that any image is taken because it
432 will be more likely that an overpass occurs on a clear or semi-clear day. While satellite
433 constellations may help improve the revisit interval, the calibration drift greatly affects retrieval
434 accuracy (Figure 8) and would need to be included in the uncertainty propagation of retrievals
435 from satellite constellations.

436 The SBG mission is driven by the ideals of the decadal survey, striving to better understand the
437 changing geophysical properties across the Earth system (National Academies of Sciences,
438 Engineering, and Medicine, 2019). We have shown the dominant components that drive retrieval
439 uncertainty across four core scientific areas. Our approach utilizes a workflow for simulating the
440 SNR effects of mission instruments and includes many aspects of data processing uncertainties.
441 Future work may focus on using this type of setup for mission planning where simulations may
442 be run to parse out different dominant contributors of uncertainty. For example, intrinsic
443 dimensionality can provide an algorithm agnostic evaluation approach by focusing simply on
444 information content (Cawse-Nicholson et. al, 2019). Once the mission design has been finalized
445 our method can be used to inform the data pipeline from SBG or future hyperspectral missions
446 by applying realistic uncertainties along the data processing steps.

447 **Acknowledgments**

448 Some of the research described in this paper was carried out at the Jet Propulsion Laboratory,
449 California Institute of Technology, under contract with the National Aeronautics and Space
450 Administration. Government sponsorship acknowledged. We acknowledge funding from
451 NASA's Surface Biology and Geology Designated Observable.

452 **Open Research Statement**

453
454 The data used in this work are hyperspectral images collected from past published works (Listed
455 in Table 1). The software used in this work is ISOFIT
456 (<https://doi.org/10.5281/ZENODO.4614338>), HYPERTRACE

457 (<https://github.com/isofit/isofit/tree/master/examples/py-hypertrace>), and four types of
458 hyperspectral algorithms (See Table 1).

459 **References**

- 460 Bioucas-Dias, J. M., & Nascimento, J. M. P. (2005). Estimation of signal subspace on hyperspectral data.
461 In L. Bruzzone (Ed.) (p. 59820L). Presented at the Remote Sensing, Bruges, Belgium.
462 <https://doi.org/10.1117/12.620061>
- 463 Burnett, A. C., Anderson, J., Davidson, K. J., Ely, K. S., Lamour, J., Li, Q., et al. (2021). A best-practice
464 guide to predicting plant traits from leaf-level hyperspectral data using partial least squares
465 regression. *Journal of Experimental Botany*, 72(18), 6175–6189. <https://doi.org/10.1093/jxb/erab295>
- 466 Cavender-Bares, J., Gamon, J. A., & Townsend, P. A. (Eds.). (2020). Remote sensing of plant
467 biodiversity. Cham: Springer.
- 468 Cawse-Nicholson, K., Hook, S. J., Miller, C. E., & Thompson, D. R. (2019). Intrinsic Dimensionality in
469 Combined Visible to Thermal Infrared Imagery. *IEEE Journal of Selected Topics in Applied Earth
470 Observations and Remote Sensing*, 12(12), 4977–4984. <https://doi.org/10.1109/JSTARS.2019.2938883>
- 471 Cawse-Nicholson, K., Townsend, P. A., Schimel, D., Assiri, A. M., Blake, P. L., Buongiorno, M. F., et al.
472 (2021). NASA's surface biology and geology designated observable: A perspective on surface imaging
473 algorithms. *Remote Sensing of Environment*, 257, 112349. <https://doi.org/10.1016/j.rse.2021.112349>
- 474 Chadwick, K. D., Brodrick, P. G., Grant, K., Goulden, T., Henderson, A., Falco, N., et al. (2020).
475 Integrating airborne remote sensing and field campaigns for ecology and Earth system science. *Methods
476 in Ecology and Evolution*, 11(11), 1492–1508. <https://doi.org/10.1111/2041-210X.13463>
- 477 Committee on Extreme Weather Events and Climate Change Attribution, Board on Atmospheric Sciences
478 and Climate, Division on Earth and Life Studies, & National Academies of Sciences, Engineering, and
479 Medicine. (2016). Attribution of Extreme Weather Events in the Context of Climate Change. Washington,
480 D.C.: National Academies Press. <https://doi.org/10.17226/21852>
- 481 Connelly, D. S., Thompson, D. R., Mahowald, N. M., Li, L., Carmon, N., Okin, G. S., & Green, R. O.
482 (2021). The EMIT mission information yield for mineral dust radiative forcing. *Remote Sensing of
483 Environment*, 258, 112380. <https://doi.org/10.1016/j.rse.2021.112380>
- 484 Curran, P. J. (1989). Remote sensing of foliar chemistry. *Remote Sensing of Environment*, 30(3), 271–
485 278. [https://doi.org/10.1016/0034-4257\(89\)90069-2](https://doi.org/10.1016/0034-4257(89)90069-2)
- 486 Dierssen, H. M. (2021). Corrigendum: Hyperspectral Measurements, Parameterizations, and Atmospheric
487 Correction of Whitecaps and Foam From Visible to Shortwave Infrared for Ocean Color Remote
488 Sensing. *Frontiers in Earth Science*, 9, 683136. <https://doi.org/10.3389/feart.2021.683136>
- 489 Dozier, J., & Painter, T. H. (2004). Multispectral and hyperspectral remote sensing of alpine snow
490 properties. *Annual Review of Earth and Planetary Sciences*, 32(1), 465–494.
491 <https://doi.org/10.1146/annurev.earth.32.101802.120404>
- 492 Garcia, R. A., Lee, Z., Barnes, B. B., Hu, C., Dierssen, H. M., & Hochberg, E. J. (2020). Benthic
493 classification and IOP retrievals in shallow water environments using MERIS imagery. *Remote Sensing
494 of Environment*, 249, 112015. <https://doi.org/10.1016/j.rse.2020.112015>

- 495 German Aerospace Center (DLR). Available at: <https://geoservice.dlr.de/data-assets/hxom21uqeo90.html>
496 (Accessed: 8 December 2021).
- 497 Hu, C. (2011). An empirical approach to derive MODIS ocean color patterns under severe sun
498 glint. *Geophysical Research Letters*, 38(1), n/a-n/a. <https://doi.org/10.1029/2010GL045422>
- 499 Isofit, Brodrick, P., Erickson, A., Jfahlen, Winstonolson, Thompson, D. R., et al. (2021). isofit/isofit:
500 2.8.0 (Version v2.8.0). Zenodo. <https://doi.org/10.5281/ZENODO.4614338>
- 501 Kokaly, R. F., Asner, G. P., Ollinger, S. V., Martin, M. E., & Wessman, C. A. (2009). Characterizing
502 canopy biochemistry from imaging spectroscopy and its application to ecosystem studies. *Remote*
503 *Sensing of Environment*, 113, S78–S91. <https://doi.org/10.1016/j.rse.2008.10.018>
- 504 National Academies of Sciences, Engineering, and Medicine (U.S.), National Academies of Sciences,
505 Engineering, and Medicine (U.S.), & National Academies of Sciences, Engineering, and Medicine (U.S.)
506 (Eds.). (2018). *Thriving on our changing planet: a decadal strategy for Earth observation from space*.
507 Washington, DC: The National Academies Press.
- 508 Nolin, A. W., & Dozier, J. (1993). Estimating snow grain size using AVIRIS data. *Remote Sensing of*
509 *Environment*, 44(2–3), 231–238. [https://doi.org/10.1016/0034-4257\(93\)90018-S](https://doi.org/10.1016/0034-4257(93)90018-S)
- 510 Schaepman-Strub, G., Schaepman, M. E., Painter, T. H., Dangel, S., & Martonchik, J. V. (2006).
511 Reflectance quantities in optical remote sensing—definitions and case studies. *Remote Sensing of*
512 *Environment*, 103(1), 27–42. <https://doi.org/10.1016/j.rse.2006.03.002>
- 513 Schimel, D., Townsend, P. A. and Pavlick, R. (2020) ‘Prospects and Pitfalls for Spectroscopic Remote
514 Sensing of Biodiversity at the Global Scale’, in Cavender-Bares, J., Gamon, J. A., and Townsend, P. A.
515 (eds) *Remote Sensing of Plant Biodiversity*. Cham: Springer International Publishing, pp. 503–518.
- 516 Serbin, Shawn P., and Philip A. Townsend. "Scaling functional traits from leaves to canopies." *Remote*
517 *Sensing of Plant Biodiversity*. Springer, Cham, 2020. 43-82.
- 518 Stavaros et al. (In Review) ‘Designing an Observing System to Study the Surface Biology and Geology of
519 the Earth in the 2020s’, *Journal of Geophysical Research: Biogeosciences*
- 520 Shiklomanov, A. N., Dietze, M. C., Viskari, T., Townsend, P. A., & Serbin, S. P. (2016). Quantifying the
521 influences of spectral resolution on uncertainty in leaf trait estimates through a Bayesian approach to
522 RTM inversion. *Remote Sensing of Environment*, 183, 226–238.
523 <https://doi.org/10.1016/j.rse.2016.05.023>
- 524 Skiles, S. M., & Painter, T. (2017). Daily evolution in dust and black carbon content, snow grain size, and
525 snow albedo during snowmelt, Rocky Mountains, Colorado. *Journal of Glaciology*, 63(237), 118–132.
526 <https://doi.org/10.1017/jog.2016.125>
- 527 Song, C., Woodcock, C. E., Seto, K. C., Lenney, M. P., & Macomber, S. A. (2001). Classification and
528 Change Detection Using Landsat TM Data. *Remote Sensing of Environment*, 75(2), 230–244.
529 [https://doi.org/10.1016/S0034-4257\(00\)00169-3](https://doi.org/10.1016/S0034-4257(00)00169-3)
- 530 Swayze, G. A., Clark, R. N., Goetz, A. F. H., Livo, K. E., Breit, G. N., Kruse, F. A., et al. (2014).
531 Mapping Advanced Argillic Alteration at Cuprite, Nevada, Using Imaging Spectroscopy. *Economic*
532 *Geology*, 109(5), 1179–1221. <https://doi.org/10.2113/econgeo.109.5.1179>
- 533 Swayze, Gregg A. (2003). Effects of spectrometer band pass, sampling, and signal-to-noise ratio on

- 534 spectral identification using the Tetracorder algorithm. *Journal of Geophysical Research*, 108(E9), 5105.
535 <https://doi.org/10.1029/2002JE001975>
- 536 Thompson, D. R., Boardman, J. W., Eastwood, M. L., & Green, R. O. (2017). A large airborne survey of
537 Earth's visible-infrared spectral dimensionality. *Optics Express*, 25(8), 9186.
538 <https://doi.org/10.1364/OE.25.009186>
- 539 Thompson, D. R., Hochberg, E. J., Asner, G. P., Green, R. O., Knapp, D. E., Gao, B.-C., et al. (2017).
540 Airborne mapping of benthic reflectance spectra with Bayesian linear mixtures. *Remote Sensing of*
541 *Environment*, 200, 18–30. <https://doi.org/10.1016/j.rse.2017.07.030>
- 542 Thompson, D. R., Natraj, V., Green, R. O., Helmlinger, M. C., Gao, B.-C., & Eastwood, M. L. (2018).
543 Optimal estimation for imaging spectrometer atmospheric correction. *Remote Sensing of*
544 *Environment*, 216, 355–373. <https://doi.org/10.1016/j.rse.2018.07.003>
- 545 Thompson, D. R., Bearden, D., Brosnan, I., Cawse-Nicholson, K., Chroné, J., Green, R. O., et al. (2021).
546 NASA's Surface Biology and Geology Concept Study: Status and Next Steps. In 2021 IEEE International
547 Geoscience and Remote Sensing Symposium IGARSS (pp. 112–114). Brussels, Belgium: IEEE.
548 <https://doi.org/10.1109/IGARSS47720.2021.9554480>
- 549 Turner, M. G., Dale, V. H., & Gardner, R. H. (1989). Predicting across scales: Theory development and
550 testing. *Landscape Ecology*, 3(3–4), 245–252. <https://doi.org/10.1007/BF00131542>
- 551 Vermote, E. F., & Kotchenova, S. (2008). Atmospheric correction for the monitoring of land
552 surfaces. *Journal of Geophysical Research*, 113(D23), D23S90. <https://doi.org/10.1029/2007JD009662>
- 553 Verrelst, J., Malenovsky, Z., Van der Tol, C., Camps-Valls, G., Gastellu-Etchegorry, J.-P., Lewis, P., et
554 al. (2019). Quantifying Vegetation Biophysical Variables from Imaging Spectroscopy Data: A Review on
555 Retrieval Methods. *Surveys in Geophysics*, 40(3), 589–629. <https://doi.org/10.1007/s10712-018-9478-y>
- 556 Wang, R., Gamon, J. A., Cavender-Bares, J., Townsend, P. A., & Zyguelbaum, A. I. (2018). The spatial
557 sensitivity of the spectral diversity–biodiversity relationship: an experimental test in a prairie
558 grassland. *Ecological Applications*, 28(2), 541–556. <https://doi.org/10.1002/eap.1669>
- 559 Wang, Z., Chlus, A., Geygan, R., Ye, Z., Zheng, T., Singh, A., et al. (2020). Foliar functional traits from
560 imaging spectroscopy across biomes in eastern North America. *New Phytologist*, 228(2), 494–511.
561 <https://doi.org/10.1111/nph.16711>
- 562 Zheng, T. *et al.* (in prep) 'Variability in forest plant traits along the Western Ghats of India and their
563 environmental drivers at different resolutions', *The New Phytologist*.